

Removing Pixel Noises and Spatial Artifacts with Generative Diversity Denoising Methods

Mangal Prakash
CSBD/ Max-Planck Institute CBG
prakash@mpi-cbg.de

Mauricio Delbracio
Google Research
mdelbra@google.com

Peyman Milanfar
Google Research
milanfar@google.com

Florian Jug
CSBD/ Max-Planck Institute CBG
Fondazione Human Technopole
jug@mpi-cbg.de, florian.jug@fht.org

Abstract

Image denoising and artefact removal are complex inverse problems admitting many potential solutions. Variational Autoencoders (VAEs) can be used to learn a whole distribution of sensible solutions, from which one can sample efficiently. However, such a generative approach to image restoration is only studied in the context of pixel-wise noise removal (e.g. Poisson or Gaussian noise). While important, a plethora of application domains suffer from imaging artefacts (structured noises) that alter groups of pixels in correlated ways. In this work we show, for the first time, that generative diversity denoising (GDD) approaches can learn to remove structured noises without supervision. To this end, we investigate two existing GDD architectures, introduce a new one based on hierarchical VAEs, and compare their performances against a total of seven state-of-the-art baseline methods on five sources of structured noise (including tomography reconstruction artefacts and microscopy artefacts). We find that GDD methods outperform all unsupervised baselines and in many cases not lagging far behind supervised results (in some occasions even superseding them). In addition to structured noise removal, we also show that our new GDD method produces new state-of-the-art (SOTA) results on seven out of eight benchmark datasets for pixel-noise removal. Finally, we offer insights into the daunting question of how GDD methods distinguish structured noise, which we like to see removed, from image signals, which we want to see retained.

1. Introduction

Image restoration is a fundamental problem in computer vision. All image data, from regular photographs to microscopy or medical images, are subject to unwanted noise

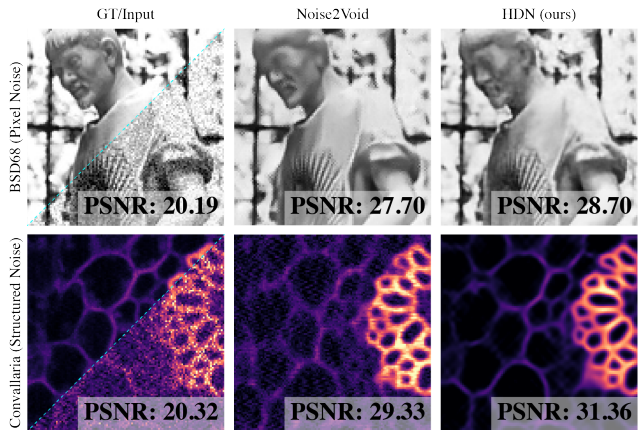


Figure 1. **HIERARCHICAL DIVNOISING (HDN) for pixel-wise and structured noise removal.** We show ground truth and noisy input (left), the result of a well known unsupervised baseline method (middle), and the MMSE result obtained with HIERARCHICAL DIVNOISING (right). The top row is subject to pixel-noise, *i.e.* Gaussian noise, while the bottom row is a real-world microscopy image subject to pixel-noise and spatially correlated structured noise (faint horizontal striping artefacts).

and artefacts. Often the most dominant sources of noise are pixel-noises such as Gaussian and Poisson noise [30]. We distinguish pixel-noises from structured noises, *i.e.* all signal corruptions or artefacts that affect groups of pixels in correlated ways.

Supervised image restoration methods based on Deep Learning (DL) can address pixel-wise and structured noises but require paired training data that allows the trained network to distinguish wanted signal from unwanted corruption patterns [56, 54, 33, 8, 16]. The applicability of unsupervised methods is much broader since they do not require paired training data [29, 2, 42, 30, 31, 51], but their downsides are that (*i*) most of them are only capable of re-

moving pixel-noises, and (ii) they typically show weaker overall performance than their supervised alternatives.

Generative Diversity Denoising (GDD) methods such as [40, 39] have recently been proposed for unsupervised denoising. Additional to producing state-of-the-art (SOTA) results on many denoising benchmarks [40], GDD methods can generate diverse denoised solutions, giving users access to samples from a distribution of sensible denoising results. The most impressive results are, so far, reported on limited image domains such as microscopy datasets and photographs of human faces. On richer domains, *e.g.* natural images, the expressivity of the employed generative models becomes a bottleneck [40]. Additionally, GDD methods are so far not used to remove structured noises.

In this work, we first introduce a new GDD method called HIERARCHICAL DIVNOISING (HDN). HDN employs hierarchical VAEs and, as we show on eight publicly available benchmark datasets from diverse image domains, is the new SOTA method for pixel-noise removal.

We then study GDD methods based on Variational Autoencoders (VAEs) with respect to their ability to perform unsupervised structured noise removal. More specifically, we investigate if and how well VAE-GDD methods can learn to remove various sources of patterned artefacts from input images without supervision. Our experiments include simulated structured noises, real-world microscopy artefacts, and structured noise introduced during computed tomography (CT) reconstruction. We show, for the first time, that GDD methods can indeed be used to remove complex artefacts from noisy data. While this is known to not be possible with other unsupervised methods [29, 2, 42, 31], it immediately raises the question how GDD methods distinguish between structured noise, which should be removed, from true image signals, which need to be retained.

To provide some answers to this fundamental question, we perform a series of experiments and analyses, leading us to identifying several factors that contribute to successful artefact removal using GDD methods. We believe these analyses are important initial steps towards interpretable image restoration with GDDs.

2. Related Work

Image restoration without deep learning (DL). Next to classical methods such as bilateral filtering [50] or Wiener filtering [17], arguably the most popular non DL based methods are Non-Local Means [7] and BM3D [15]. Non-Local Means uses information from similar regions in the image to obtain estimates of the underlying clean pixel values while BM3D uses a two stage non-locally collaborative filtering. A detailed review of classical denoising methods can be found in [37].

Image restoration with supervised DL. Supervised DL

methods using paired training data have been shown to perform extraordinary well for many image restoration tasks [56, 54, 33, 16, 9]. These methods can be used to remove pixel-noises and structured noise (artefacts) since the provided image pairs showcase which visible structures are wanted and which ones are not. However, paired training data is typically not available and can be hard or even impossible to obtain [8, 9].

Image restoration with unsupervised DL. Ulyanov *et al.* [51] showed that convolutional neural networks (CNNs) can be used to restore corrupted images without supervision when training is stopped at an a priori unknown time before convergence. Their method, called Deep Image Prior (DIP), is extraordinarily interesting in that it demonstrates an existing inductive bias (prior) of CNNs. Methods such as DIP (or other methods that require training for each input image separately, *e.g.* SELF2SELF [42]) are, however, computationally very expensive. To address these problems, an array of methods was proposed [29, 2, 55, 30, 31], all of them addressing pixel-noise removal, exclusively. Broadus *et al.* [4] extend [29] and show how structured line artefacts that are common for certain microscopy modalities can be removed.

Image restoration with generative DL methods. Generative Adversarial Networks (GANs) [20] and Variational Autoencoders (VAEs) [27, 44] are powerful generative models. GANs have, for example, been used to generate pairs of noisy and clean images, later used to train supervised denoising networks [11]. Another interesting approach to image restoration on unpaired training data using GANs is [36].

Although VAEs do not explicitly address denoising, the output of a VAE decoder can be interpreted as predicting a Gaussian noise distribution per pixel. Prakash *et al.* [40] make the link between VAEs and denoising more explicit and more practical by introducing a suitable pixel-noise model in the decoder.

Hierarchical VAEs. Hierarchical VAEs [48, 35] are splitting the latent space encoding into multiple conditionally dependent latent (sub-)spaces. This can greatly improve the expressivity of VAEs, recently demonstrated on high-resolution image generation tasks [52, 13]. In this work we draw inspiration from several works [48, 35, 52, 13] in order to propose HIERARCHICAL DIVNOISING, an improved method for diversity denoising.

3. The Image Restoration Task

The task of image restoration involves the estimation of a clean and unobservable signal $\mathbf{s} = (s_1, s_2, \dots, s_N)$ from a corrupted reconstruction $\mathbf{x} = (x_1, x_2, \dots, x_N)$, where s_i and x_i , refer to the respective pixel intensities in the image domain. In general, the reconstructed image comes from

solving an inverse imaging problem giving by the forward model,

$$\mathbf{y} = A(\mathbf{s}) + \mathbf{e}, \quad (1)$$

where A is the forward operator (tomography, blurring, sub-sampling, etc), \mathbf{e} is noise in the measurements typically assumed iid, and \mathbf{y} is the noisy measurements. An image reconstruction algorithm is needed to recover an estimation \mathbf{x} of \mathbf{s} from the noisy measurements \mathbf{y} . Typically, the image reconstruction is obtained through an optimization formulation, where we seek a solution \mathbf{x} that fits the observed values and is compatible with some image prior R ,

$$\mathbf{x} = \arg \min_{\mathbf{s}} \|A(\mathbf{s}) - \mathbf{y}\|^2 + \lambda R(\mathbf{s}).$$

The parameter $\lambda \geq 0$ is related to the level of confidence in the prior R . There exists an extensive amount of work defining image priors [47, 18, 5, 57, 45, 51].

Without loss of generality, we can decompose the reconstructed image as

$$\mathbf{x} = \mathbf{s} + \mathbf{n}, \quad (2)$$

where \mathbf{n} is the residual (noise) between the ideal image and the reconstructed one. Generally, the *noise* \mathbf{n} on the reconstruction \mathbf{x} is composed of pixel-noise (such as Poisson or Gaussian noise) and multi-pixel artefacts or structured noise that affect groups of pixels in correlated ways. Such artefacts arise through dependencies that are introduced by the adopted reconstruction technique and the domain-specific inverse problem (*e.g.* tomography, microscopy, or ISP in an optical camera).

In Section 5 we make the assumption that the noise contribution n_i to each pixel x_i is conditionally independent given the signal s_i , *i.e.* $p(\mathbf{n}|\mathbf{s}) = \prod_i p(n_i|s_i)$ [29].

In many practical applications, including the ones presented in Section 6, this assumption does unfortunately not hold true, and the noise \mathbf{n} is harder to formally grasp. This is equally true for supervised image restoration approaches, but by having access to paired image data with fixed \mathbf{s} and changing \mathbf{n} , a distinction between wanted and unwanted structures can be learned [53, 33, 8].

4. Generative Diversity Denoising (GDD)

GDD methods grant access to diverse restorations by means of providing samples s^k drawn from a posterior distribution of restored images. More formally, the restoration operation of a GDD model can be expressed by $f_\psi(\mathbf{x}) = s^k \sim p(\mathbf{s}|\mathbf{x})$, where f is a GDD model with parameters ψ . In this work, we propose a new GDD method called HIERARCHICAL DIVNOISING and compare it with two existing GDD methods, namely DIVNOISING [40] and vanilla VAEs [27, 44].

Vanilla VAEs. VAEs are generative encoder-decoder models, capable of learning a latent representation of the data

and capturing a distribution over inputs \mathbf{x} [28, 21]. The encoder maps input \mathbf{x} to a conditional distribution $q_\phi(\mathbf{z}|\mathbf{x})$ in latent space. The decoder, $g_\theta(\mathbf{z})$, takes a sample from $q_\phi(\mathbf{z}|\mathbf{x})$ and maps it to a distribution $p_\theta(\mathbf{x}|\mathbf{z})$ in image space. Encoder and decoder are neural networks, jointly trained to minimize the loss

$$\mathcal{L}_{\phi,\theta}(\mathbf{x}) = \mathbb{E}_{q_\phi(\mathbf{z}|\mathbf{x})}[-\log p_\theta(\mathbf{x}|\mathbf{z})] + \mathbb{KL}(q_\phi(\mathbf{z}|\mathbf{x})||p(\mathbf{z})), \quad (3)$$

with the second term being the KL-divergence between the encoder distribution $q_\phi(\mathbf{z}|\mathbf{x})$ and prior distribution $p(\mathbf{z})$ (usually a unit normal distribution). The network parameters of the encoder and decoder are given by ϕ and θ , respectively. The decoder is usually modelled to factorize over pixels as

$$p_\theta(\mathbf{x}|\mathbf{z}) = \prod_{i=1}^N p_\theta(x_i|\mathbf{z}), \quad (4)$$

with $p_\theta(x_i|\mathbf{z})$ being a normal distribution predicted by the decoder. The encoder distribution is modeled in a similar way, factorizing over the dimensions of the latent space \mathbf{z} .

In [40] the performance of vanilla VAEs on pixel-noise removal tasks was analyzed, and an improved method called DIVNOISING was introduced.

DIVNOISING (DN). DN [40] is a VAE based method for unsupervised pixel noise removal that incorporates an explicit noise model $p_{\text{NM}}(\mathbf{x}|\mathbf{s})$ in the decoder. More formally, the generic normal distribution over pixel intensities of Eq. 4 is replaced with a known noise model $p_{\text{NM}}(\mathbf{x}|\mathbf{s})$ which factorizes as a product of pixels, *i.e.* $p_{\text{NM}}(\mathbf{x}|\mathbf{s}) = \prod_i^N p_{\text{NM}}(x_i|s_i)$, and the decoder learns a mapping from \mathbf{z} directly to the space of restored images, *i.e.* $g_\theta(\mathbf{z}) = \mathbf{s}$. Therefore,

$$p_\theta(\mathbf{x}|\mathbf{z}) = p_{\text{NM}}(\mathbf{x}|g_\theta(\mathbf{z})). \quad (5)$$

The loss of DN hence becomes

$$\mathcal{L}_{\phi,\theta}(\mathbf{x}) = \mathbb{E}_{q_\phi(\mathbf{z}|\mathbf{x})} \left[\sum_{i=1}^N -\log p(x_i|g_\theta(\mathbf{z})) \right] + \mathbb{KL}(q_\phi(\mathbf{z}|\mathbf{x})||p(\mathbf{z})). \quad (6)$$

DN is the current SOTA for many unsupervised denoising benchmarks, but can have difficulties to learn a good posterior distribution of clean data for complex domains such as natural images [40].

HIERARCHICAL DIVNOISING. One of our contributions in this work is a new GDD method based on hierarchical VAEs [48, 35, 52, 13]. HIERARCHICAL DIVNOISING (HDN) splits its latent representation over $n > 1$ hierarchically dependent stochastic latent variables $\mathbf{z} = \{\mathbf{z}_1, \mathbf{z}_2, \dots, \mathbf{z}_n\}$. As in [13], \mathbf{z}_1 is the bottom-most latent variable, seeing the input essentially in unaltered form. The top-most latent variable is \mathbf{z}_n , receiving an $n - 1$ times

downsampled input and starting a cascade of latent variable conditioning back down the hierarchy. This architecture follows the description in [48, 34], with the *bottom-up* and *top-down* networks having parameters ϕ and θ , respectively. The *top-down* network performs a downward pass to compute a hierarchical prior $p_\theta(\mathbf{z})$ which factorizes as

$$p_\theta(\mathbf{z}) = p_\theta(\mathbf{z}_n) \prod_{i=1}^{n-1} p_\theta(\mathbf{z}_i | \mathbf{z}_{j>i}), \quad (7)$$

with each factor $p_\theta(\mathbf{z}_i | \mathbf{z}_{j>i})$ being a learned multivariate Normal distribution with diagonal covariance, and $\mathbf{z}_{j>i}$ referring to all \mathbf{z}_j with $j > i$. Note that even $p_\theta(\mathbf{z}_n)$, the prior of the top-most layer, is being learned during training.

Given a noisy input \mathbf{x} , the encoder distribution $q_\phi(\mathbf{z}|\mathbf{x})$ is computed in two steps. First the *bottom-up* network performs a deterministic upward pass and extracts representations from noisy input \mathbf{x} at each layer. Next, the representations extracted by the *top-down* network during the downward pass are merged with results from the *bottom-up* network before inferring the conditional distribution

$$q_\phi(\mathbf{z}|\mathbf{x}) = q_\phi(\mathbf{z}_n|\mathbf{x}) \prod_i^{n-1} q_{\phi,\theta}(\mathbf{z}_i | \mathbf{z}_{j>i}, \mathbf{x}). \quad (8)$$

As in DN, the conditional distribution $p_\theta(\mathbf{x}|\mathbf{z})$ is described in Eq. 5. The generative model along with the prior $p_\theta(\mathbf{z})$ and noise model $p_{\text{NM}}(\mathbf{x}|\mathbf{s})$ describes the joint distribution $p_\theta(\mathbf{z}, \mathbf{x}, \mathbf{s}) = p_{\text{NM}}(\mathbf{x}|\mathbf{s})p_\theta(\mathbf{s}|\mathbf{z})p_\theta(\mathbf{z})$. Considering Eq. 5 and 7, the denoising loss function for HDN thus becomes

$$\begin{aligned} \mathcal{L}_{\phi,\theta}(\mathbf{x}) = & \mathbb{E}_{q_\phi(\mathbf{z}|\mathbf{x})} \left[\sum_{i=1}^N -\log p(x_i | g_\theta(\mathbf{z})) \right] + \\ & \mathbb{KL}(q_\phi(\mathbf{z}_n|\mathbf{x}) || p_\theta(\mathbf{z}_n)) + \\ & \sum_{i=1}^{n-1} \mathbb{E}_{q_\phi(\mathbf{z}_{j>i}|\mathbf{x})} [\mathbb{KL}(q_{\phi,\theta}(\mathbf{z}_i | \mathbf{z}_{j>i}, \mathbf{x}) || p_\theta(\mathbf{z}_i | \mathbf{z}_{j>i}))]. \quad (9) \end{aligned}$$

Following the suggestions in [52, 13], we use residual blocks in the encoder and decoder. Additionally, as proposed in [35, 34], our generative path uses skip connections which enforce conditioning on all layers above. To avoid *KL-vanishing* [3], we use the so called *free-bits* approach [26, 12], which defines a threshold on the KL term in Eq. 9 and then only uses this term if its value is above it. A schematic of our fully convolutional network architecture is shown in Appendix A.

5. Application: Pixel-noise Removal

Datasets. We consider 8 publicly available denoising benchmark datasets from different image domains, including natural images, microscopy data, images of faces and

digits. Some of these datasets are synthetically corrupted with pixel-noise while others are intrinsically noisy. A qualitative noisy sample from each dataset is shown in Fig. 2. Appendix A.1 describes all datasets in more detail.

Baselines. We compare HDN on all datasets against (i) 7 unsupervised baseline methods, *i.e.* BM3D [15], Deep Image Prior (DIP) [51], SELF2SELF (S2S) [42], NOISE2VOID (N2V) [29], Probabilistic NOISE2VOID (PN2V) [30], NOISE2SAME [55], and DIVNOISING (DN) [40], and (ii) against 2 supervised methods, namely NOISE2NOISE (N2N) [33] and CARE [54].

Note that we are limiting the evaluation of DIP and S2S to 3 and 2 datasets, respectively. This is motivated by the prohibitive training time of these methods (training is required for each input image).

All training parameters for N2V, PN2V, DN, N2N and CARE are as reported in [29, 40, 30, 19]. NOISE2SAME, SELF2SELF and DIP are trained using the default parameters mentioned in [55], [42] and [51], respectively.

HDN Training and Denoising. All but one HDN networks make use of 6 stochastic latent variables $\mathbf{z}_1, \dots, \mathbf{z}_6$. The one exception holds for the *MNIST* dataset, where we only use 3 latent variables. Each \mathbf{z}_i has 32 dimensions per pixel. We use an initial learning rate of 0.0003 and always train for 22 million steps using Adam [25]. During training, we extract random patches from the training data (128×128 patches for *BioID Faces* and natural image datasets, 256×256 patches for *CelebA HQ*, 28×28 patches for *MNIST*, and 64×64 patches for all other datasets). Additional training details can be found in Appendix A.

All denoising results are quantified in terms of Peak-Signal-to-Noise Ratio (PSNR) against available ground truth (GT) in Table 1. MMSE results of HDN are obtained by averaging 100 diverse denoised samples per noisy input. HDN outperforms all unsupervised baselines on all dataset, only for the *Set12* data being marginally outperformed by BM3D. Note also that on 4 datasets HDN even outperforms both supervised baselines. Results with other denoising metrics are shown in Appendix I and show similar overall trend.

Expressivity of Learned Posteriors. The generator of GDD methods can naturally be used for de-novo image generation. We compare images generated by DN and HDN with real image patches and find that HDN generated images are resembling the quality of real images to a much higher degree. Results are shown in Appendix C. This demonstrates that HDN learns a more accurate posterior distribution over clean images than DN, explaining also why HDN pixel-denoising results are so much better.

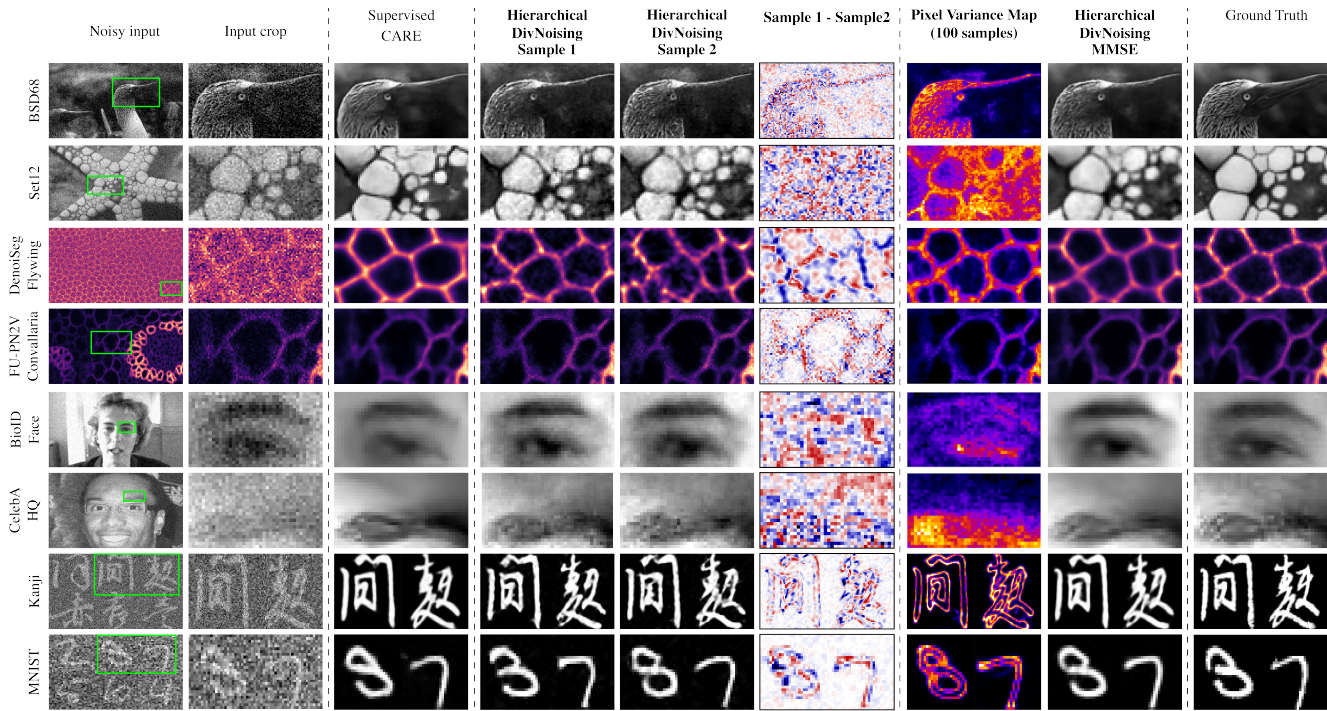


Figure 2. **Qualitative pixel-noise removal with HIERARCHICAL DIVNOISING (HDN).** For each dataset we tested (rows), we show denoising results for one representative input image. Columns show, from left to right, the input image and an interesting crop region, results of CARE, two randomly chosen HDN samples, a difference map between those samples, the per-pixel variance of 100 diverse samples, the MMSE estimate derived by averaging these 100 samples, and the ground truth image.

Dataset	Non DL	Single Image DL		Multi Image DL (non-GDD)			GDD Methods		Supervised	
	BM3D	DIP	S2S	N2V	Noise2Same	PN2V	DN	HDN (Ours)	N2N	CARE
Convallaria [41]	35.45	-	-	35.73	36.46	36.47	36.90	<u>37.10</u>	36.85	36.71
Flying [10]	23.45	24.67	-	24.79	22.81	24.85	25.02	25.41	25.67	<u>25.79</u>
BSD68 [46]	28.56	27.96	28.61	27.70	27.95	28.46	27.42	28.70	28.86	<u>29.07</u>
Set12 [56]	29.94	28.60	29.51	28.92	29.35	29.61	28.24	29.80	30.04	<u>30.36</u>
BioID Faces [1]	33.91	-	-	32.34	34.05	33.76	33.12	34.61	35.04	<u>35.06</u>
CelebA HQ [24]	33.28	-	-	30.80	31.82	33.01	31.41	33.74	33.39	33.57
MNIST [32]	15.82	-	-	19.04	18.79	13.87	19.06	<u>21.21</u>	20.29	20.43
Kanji [14]	20.45	-	-	19.95	20.28	19.40	19.47	<u>20.68</u>	20.56	20.64

Table 1. **Quantitative pixel-noise removal with HDN.** For all conducted experiments, we compare results in terms of Peak signal-to-noise ratio (PSNR in dB). The best performing method is indicated by being underlined, best performing unsupervised method is shown in bold. For all but one dataset, our HIERARCHICAL DIVNOISING is the new unsupervised SOTA method, even superseding the competing supervised baselines on 4 of the 8 used datasets.

6. Application: Structured Noise Removal

In this section, we ask if, and to what degree, GDD models can be used for image restoration, *i.e.* to remove artefacts spanning multiple pixels (structured noise). To the best of our knowledge, we are the first to ask this question. Please note that none of the GDD methods described in Sec. 4 are devised with the intention of removing structured noise. We observe that all three methods are capable of removing structured noises, raising the question why this is the case.

Striping Artefacts in Microscopy. Additional to pixel-noise, microscopy images are often subject to line artefacts [4]. These undesired patterns are not removed using unsupervised non GDD methods (see Fig. 1).

We tested vanilla VAEs, DN, and HDN on the microscopy dataset from [4], which is subject to intrinsic pixel-noise as well as said striping artefacts. In order to apply DN, we start by learning a pixel-wise GMM noise model as described in [41], using the available public implementation. Remember, this noise model only captures

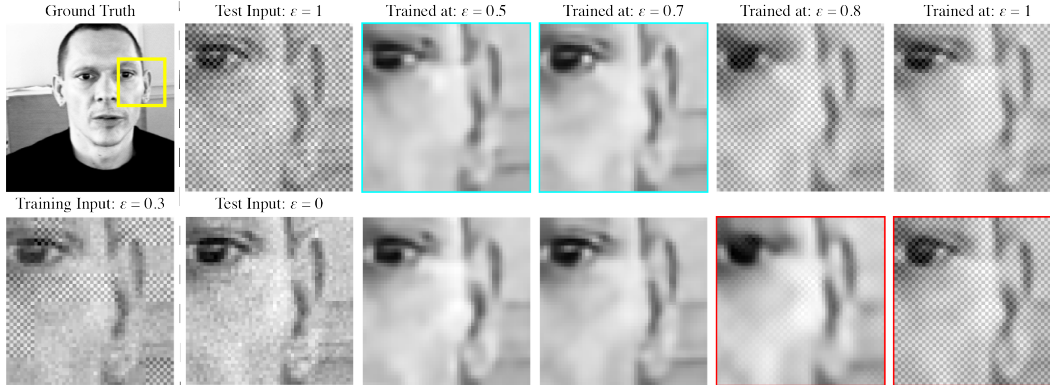


Figure 3. **Testing structured noise removal with DIVNOISING at changing artefact abundance.** The first column shows a ground truth image and below a crop of a training image subject to Gaussian noise and a superimposed chessboard patterns at an abundance of $\varepsilon = 0.3$. The second column shows two test inputs, the top one with the highest possible abundance of the chessboard patterns ($\varepsilon = 1$), while the one below does not contain this structured noise at all ($\varepsilon = 0$). The remaining 4 columns show results obtained with DIVNOISING networks trained on input data exposed to chessboard patterns at abundances ε of 0.5, 0.7, 0.8, and 1, respectively. Cyan frames in the top row indicate cases where DIVNOISING successfully removes the chessboard patterns. Red frames, in the bottom row, indicate cases where denoising results show restored chessboard patterns despite the corresponding input not containing them (*i.e.* hallucinated artefacts).

information about the pixel-noises contained in the data. Our HDN setup uses the same noise model but the more expressive hierarchical latent space, as previously described.

Results obtained by multiple baselines methods (N2V, PN2V and Struct N2V) as well as the results obtained using a vanilla VAE, DN, and HDN are shown in Table 2. We observe that both the vanilla VAE and DN outperform unsupervised baselines in terms of achieved PSNR values to the available GT. While N2V and PN2V can by design not remove structured noise, Struct N2V, however, was specifically proposed for striping artefact removal in microscopy.

It is interesting to see that HDN, which is clearly the best-performing method for pixel-denoising tasks (see Table 1), shows much worse restoration results on microscopy striping artefacts than the vanilla VAE or DN (see Table 2). To better understand why this is the case, we have first to understand why other GDD methods (vanilla VAE and DN) are capable of removing structured noises in the first place.

The very nature of VAE is to find a compact latent space encoding \mathbf{z} . By design, only what is encoded in \mathbf{z} can be reconstructed by the VAEs generator. Limiting the dimensionality of \mathbf{z} also means that the variational autoencoder needs to find a more compact representation of the image distribution it needs to capture. Since all methods minimize some pixel-wise loss, it pays to capture more dominant/frequent and larger structures over small and/or infrequent details. This is additionally facilitated by the fact that larger structures can be encoded in fewer bits (or latent space dimensions) as the very many bits it takes to encode finer structures, artefacts, or pixel-noises.

These considerations and the observations in [51] make us believe that GDD methods minimize the loss by first encoding the largest and most frequent/dominant structures into its latent code, and then successively add increasingly

finer or less abundant (but at the same time more latent space consuming) image features, only stopping once no further capacity in \mathbf{z} remains (find some additional thoughts and experimental results giving more substance to these ideas in Appendix G).

With this in mind, we can now try to understand why HDN is not performing as well as vanilla VAEs or DN on microscopy data with striping artefacts. The hierarchical latent space of HDN is simply expressive enough to not only capture larger-scale image features, but can actually even pack the slightly smaller scale striping artefacts into its encoding. Interestingly, this also means that the reason why GDD methods are capable of removing structured noises from data is essentially accidental, facilitated by insufficient expressivity/dimensionality of used latent spaces.

However, owing to its hierarchical nature, we can inspect the contributions of individual latent variables $\mathbf{z}_1, \dots, \mathbf{z}_n$ to a reconstructed image. We use the trained HDN network to visualize the image aspects captured at hierarchy levels 1 to n (see Appendix F). Maybe little surprisingly, we find that striping artefacts are (mostly) captured in \mathbf{z}_1 and \mathbf{z}_2 , the two bottom-most levels, corresponding to the highest resolution image features. With this in mind, we modified our HDN setup to compute the conditional distribution $q_{\phi, \theta}(z_i | z_{j>i}, \mathbf{x})$ of Eq. 8 only using information from the *top-down* pass, neglecting the input that is usually received from *bottom-up* computations.

Since we want to exclude artefacts which are captured in \mathbf{z}_1 and \mathbf{z}_2 we apply these modifications only to these two layers and keep all operations for layers 3 to 6 unchanged. Mentioning all layers that remain unchanged, we denote this particular setup by HDN_{3-6} . As can be seen in Table 2, the trained HDN_{3-6} network outperforms all other unsupervised methods by a rather impressive margin.

	Unsupervised non-GDD Methods			Unsupervised GDD Methods				Supervised
	N2V	PN2V	Struct N2V	Vanilla VAE	DN	HDN	HDN ₃₋₆	CARE
Struct. denoising BM [4]	29.33	29.43	30.02	30.53	31.09	29.78	31.36	31.56

Table 2. **Quantitative results for removal of striping artefacts in microscopy data.** On a real-world microscopy benchmark (Struct-Convallaria [4]), GDD methods generally outperform all unsupervised baselines in terms of peak signal-to-noise ratio (PSNR, dB). Our HDN₃₋₆ method is the new SOTA on this benchmark.

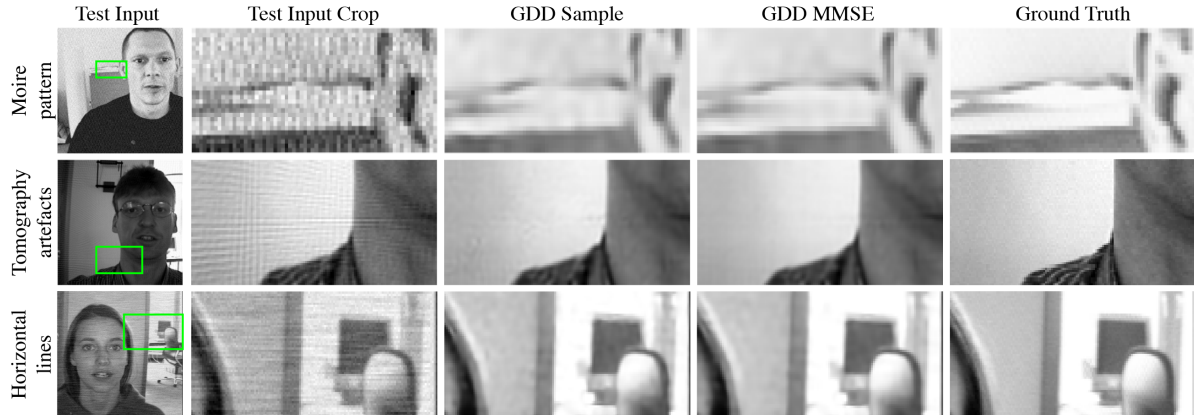


Figure 4. **Qualitative structured noise removal with GDDs.** We show image restoration results on data containing structured Moire patterns (*top row*), artefacts introduced by tomographic reconstruction (*middle row*), and horizontal line artefacts (*bottom row*). Results shown in top and bottom rows were obtained using DIVNOISING, while for the middle row we used a vanilla VAE. In each row we show the input image and a selected crop, a random sample, the MMSE result (avg of 100 samples), and corresponding ground truth crop.

Synthetic Structured Noise Experiments. With the previous experiments in mind, we want to better understand how GDD models remove structured noises and collect additional evidences for our intuitions. To this end, we take the *BioID Faces* dataset and synthetically apply structured corruptions and Gaussian pixel-noise (see Fig. 3 and Fig. 4). A detailed description of used synthetic artefacts is given in Appendix A. Next, we train DN using a noise model matching the Gaussian pixel-noise we applied while corrupting the dataset. This noise model is not in any form expressing any prior knowledge about the structured noises we have used in any of the conducted experiments.

In order to better discuss our findings, we introduce the following terminologies.

Abundance/dominance, and ε -fractions. During training, we would like to have control over the *abundance* or *dominance* of a given source of structured noise. Hence, we modulate the abundance by only corrupting an ε -fraction of all pixels of any given input image with structured noise. We then trained a series of DN networks, with training data covering a range of ε -fractions (see Fig. 3).

After training networks on various ε -fractions, we test the quality of restorations on inputs with $\varepsilon = 0$ and $\varepsilon = 1$ and empirically distinguish operational regimes separated by two observational thresholds on ε .

The encoding threshold. The *encoding threshold* is the minimal abundance of a given type of structured noise in training data so that the latent space encoding of a given GDD setup starts to capture these unwanted structures. In

other words, it is the largest ε -fraction one can use during training such that predictions made with the trained GDD network remain artefact free even for worst-case inputs, *i.e.* inputs that show the structured noise everywhere ($\varepsilon = 1$).

The hallucination threshold. While the encoding threshold tells us about how abundant artefacts need to be in order to make it into the latent space encoding of a given GDD setup, a second question to ask is when a given GDD network would start to misinterpret inputs as containing the unwanted structures even though the inputs do not have any artefacts. Hence, the *hallucination-threshold* is defined as the largest ε -fraction above which a GDD method starts to *hallucinate* these structured noises, even when applied to images not corrupted with structured noise ($\varepsilon = 0$).

In Fig. 3 we show results for a series of DN networks trained on images corrupted with Gaussian pixel-noise and structured chessboard artefacts at various ε -fractions. We observe that the *encoding threshold* and *hallucination threshold* are somewhere between 0.7 and 0.8. Results for horizontal line artefacts and Moire patterns are shown in Appendix D. We additionally look into DN networks trained with data below and above the *encoding threshold* and analyze/visualize latent space features of these networks. We find that networks either lack any representation of structured noise patterns or express those very broadly (see Appendix H).

In the top half of Table 3, we report image restoration results using DN after being trained at various ε -fractions for all three synthetic sources of structured noise. Addition-

Method	Chessboard	Horizontal	Moire
$DN_{\varepsilon = 0.01}$	33.22	35.11	32.91
$DN_{\varepsilon = 0.03}$	33.04	34.98	33.08
$DN_{\varepsilon = 0.05}$	33.06	35.04	32.93
$DN_{\varepsilon = 0.10}$	33.05	34.80	32.85
$DN_{\varepsilon = 0.50}$	32.97	34.76	28.64
$DN_{\varepsilon = 1.0}$	19.59	34.10	26.63
test input:	200 pas	180 pas	150 pas
DIP	39.84	39.48	38.74
S2S	36.19	36.05	35.29
VAE ₂₀₀	41.78	41.18	39.34
VAE ₁₈₀	41.92	41.12	39.15
VAE ₁₅₀	42.07	41.01	38.78

Table 3. **Structured noise removal with GDDs.** Top 6 rows show DIVNOISING (DN) results on the *BioID-Faces* dataset, subjected to 3 sources of structured noises (see text for details). Rows differ by the abundance (ε -fraction) of the respective structured noise during training. All results are evaluated on test-inputs generated at maximum artefact abundance ($\varepsilon = 1$). Bottom 5 rows compare results of DIP [51], S2S [42], and vanilla VAEs trained on tomographic reconstructions from either 150, 180, or 200 projection angles (pas), also indicated as subscript in column 1. While DIP and S2S is always use the same pas during training and testing, for VAE setup we evaluated all nine combinations. All numbers indicate PSNR values w.r.t. available ground truth images.

ally, we compare DN results against supervised methods NOISE2NOISE and CARE and report these results in Appendix E.

Artefact Removal in CT Reconstructions. Last but not least, we report some results on artefact removal in Computational Tomography (CT) reconstructions. To this end we have devised a synthetic CT imaging pipeline that allows us to perform in-silico CT on any given image. This has the advantage that ground truth images are known, which is typically not the case in medical CT images. Since we do not expose generated CT images to pixel-noises, we choose the vanilla VAE for our experiments. We show a qualitative result in Fig. 4 and report quantitative results on 7 randomly selected test images using our VAE setup, DIP and SELF2SELF in Table 3.

Computed tomography uses a series of 1D projection of a 2D sample (in our case a ground truth image), typically acquired from some equally spaced viewing angles. Perfect CT reconstructions using a method called *filtered backprojection* (FBP) [23, 43] can theoretically be obtained if such projections are available at sufficient density. Reducing the number of available projections gives rise to an increasing amount of streaking artefacts [6], as can be seen in Fig. 4.

Here we have no direct influence on the ε -fraction of corrupted pixels during training. Instead, we are modulating the abundance of CT artefacts by changing the number of projections used to create FBP reconstructions. Our results show that there exists a regime below a certain *encoding*

threshold where the VAE does not encode CT artefacts. Results obtained by our VAE outperform both baselines. A comparison against supervised methods is given in Appendix E.

7. Discussion

In this work, we have introduced HIERARCHICAL DIVNOISING (HDN), a new GDD method utilizing expressive hierarchical latent spaces, leading to SOTA results on 7 out of 8 unsupervised denoising benchmarks. Additionally, we showed that different layers of the hierarchical latent space encode for image features at different spatial scales. We used this to selectively “deactivate” bottom-up input to latent layers when they encode undesired structured noises. We demonstrated this approach on a real-world microscopy dataset corrupted by line-scanning artefacts, where our HDN approach produces SOTA results.

We expect that selective “deactivation” of latent layers will find practical application for many microscopy datasets corrupted with structured noise. Since microscopy data is typically diffraction limited, the pixel-resolution of micrographs typically exceeds the optical resolution of visible structures. This means that true image structures are blurred by a blur kernel called the point spread function. Hence, the spatial scale of the true signal in microscopy data is not the same as the spatial scale of many structured microscopy noises and the method we proposed for microscopy data restoration in Section 6 will likely apply.

We have then explored the capability of GDD methods to remove structured noises beyond striping artefacts. In total we experimented with 3 synthetic sources of structured noise as well as artefacts that arise by a commonly used reconstruction pipeline in computed tomography (CT). We saw that all sources of structured noise can be removed with GDD methods as long as the trained latent space does not encode the unwanted structures. To better understand our observations, we introduced *encoding threshold* and *hallucination threshold* that we used to evaluate how robustly the GDD setups we used remove the respective source of structured noise (as a function of their, as we called it, abundances).

As we have reasoned in Section 6, unsupervised removal of structured noise with GDD methods is a consequence of finding a compressed latent space encoding that can or cannot describe all observable image features contained in a given body of training data. Hence, whether or not artefacts are removed is an indirect consequence of a combination of factors that are not easily controllable, *i.e.* (i) the expressivity of the latent space, (ii) the abundance or dominance of artefacts in the training data, (iii) the predictability/complexity of the artefacts, and (iv) how much encoding the structured noise contributes to the loss used to train the GDD setup.

While, as we have shown, unsupervised GDD pixel-noise removal leads to SOTA results, for structured noise removal the situation is more complicated. Whenever the structured noise is not abundant enough to be learned by a given GDD setup, SOTA results can be achieved. Still, in order to increase the scope and practicality of GDD methods for unsupervised structured noise removal, finer grained control over what structures a GDD method picks up or ignores will be needed. In future work we will address this remaining shortcoming.

Acknowledgments

The authors would like to thank Alexander Krull and Sander Dieleman for valuable discussions during early phases of this project. We also want to thank the Scientific Computing Facility at MPI-CBG for giving us access to HPC infrastructure. Funding was provided from the Max-Planck Society under project code M.I.F.A.MOZG8106, the core budget of the Max-Planck Institute of Molecular Cell Biology and Genetics (MPI-CBG), the Human Technopole, and the BMBF under codes 031L0102 (de.NBI) and 01HS18026C (ScaDS2), as well as by the DFG under code JU3110/1-1 (FiSS).

References

- [1] BioID Face Database | Face Detection Dataset | facedb.
- [2] Joshua Batson and Loic Royer. Noise2self: Blind denoising by self-supervision, 2019.
- [3] Samuel R Bowman, Luke Vilnis, Oriol Vinyals, Andrew M Dai, Rafal Jozefowicz, and Samy Bengio. Generating sentences from a continuous space. *arXiv preprint arXiv:1511.06349*, 2015.
- [4] C. Broaddus, A. Krull, M. Weigert, U. Schmidt, and G. Myers. Removing structured noise with self-supervised blind-spot networks. In *2020 IEEE 17th International Symposium on Biomedical Imaging (ISBI)*, pages 159–163, 2020.
- [5] Alfred M Bruckstein, David L Donoho, and Michael Elad. From sparse solutions of systems of equations to sparse modeling of signals and images. *SIAM review*, 51(1):34–81, 2009.
- [6] Philippe P Bruyant, Jacques Sau, and Jean-Jacques Mallet. Streak artifact reduction in filtered backprojection using a level line-based interpolation method. *Journal of Nuclear Medicine*, 41(11):1913–1919, 2000.
- [7] Antoni Buades, Bartomeu Coll, and J-M Morel. A non-local algorithm for image denoising. In *2005 IEEE Computer Society Conference on Computer Vision and Pattern Recognition (CVPR'05)*, volume 2, pages 60–65. IEEE, 2005.
- [8] Tim-Oliver Buchholz, Mareike Jordan, Gaia Pigino, and Florian Jug. Cryo-care: Content-aware image restoration for cryo-transmission electron microscopy data. In *2019 IEEE 16th International Symposium on Biomedical Imaging (ISBI 2019)*, pages 502–506. IEEE, 2019.
- [9] Tim-Oliver Buchholz, Alexander Krull, Réza Shahidi, Gaia Pigino, Gáspár Jékely, and Florian Jug. Content-aware image restoration for electron microscopy. In Gaia Pigino and Thomas Müller-Reichert, editors, *Three-Dimensional Electron Microscopy*, pages 277–289. Academic Press, July 2019.
- [10] Tim-Oliver Buchholz, Mangal Prakash, Alexander Krull, and Florian Jug. Denoiseg: Joint denoising and segmentation. *arXiv preprint arXiv:2005.02987*, 2020.
- [11] Jingwen Chen, Jiawei Chen, Hongyang Chao, and Ming Yang. Image blind denoising with generative adversarial network based noise modeling. In *Proceedings of the IEEE Conference on Computer Vision and Pattern Recognition*, pages 3155–3164, 2018.
- [12] Xi Chen, Diederik P Kingma, Tim Salimans, Yan Duan, Prafulla Dhariwal, John Schulman, Ilya Sutskever, and Pieter Abbeel. Variational lossy autoencoder. *arXiv preprint arXiv:1611.02731*, 2016.
- [13] Rewon Child. Very deep {vae}s generalize autoregressive models and can outperform them on images. In *International Conference on Learning Representations*, 2021.
- [14] Tarin Clanuwat, Mikel Bober-Irizar, Asanobu Kitamoto, Alex Lamb, Kazuaki Yamamoto, and David Ha. Deep learning for classical japanese literature. *arXiv preprint arXiv:1812.01718*, 2018.
- [15] Kostadin Dabov, Alessandro Foi, Vladimir Katkovnik, and Karen Egiazarian. Image denoising by sparse 3-d transform-domain collaborative filtering. *IEEE Transactions on image processing*, 16(8):2080–2095, 2007.
- [16] Mauricio Delbracio, Hossein Talebi, and Peyman Milanfar. Projected distribution loss for image enhancement. *arXiv preprint arXiv:2012.09289*, 2020.
- [17] Sadeep Ghael, Akbar M Sayeed, and Richard G Baraniuk. Improved wavelet denoising via empirical wiener filtering. In *SPIE Technical Conference on Wavelet Applications in Signal Processing*, 1997.
- [18] Gene H Golub, Per Christian Hansen, and Dianne P O’Leary. Tikhonov regularization and total least squares. *SIAM journal on matrix analysis and applications*, 21(1):185–194, 1999.
- [19] Anna S Goncharova, Alf Honigmann, Florian Jug, and Alexander Krull. Improving blind spot denoising for microscopy. In *European Conference on Computer Vision*, pages 380–393. Springer, 2020.
- [20] Ian Goodfellow, Jean Pouget-Abadie, Mehdi Mirza, Bing Xu, David Warde-Farley, Sherjil Ozair, Aaron Courville, and Yoshua Bengio. Generative adversarial nets. In *Advances in neural information processing systems*, pages 2672–2680, 2014.
- [21] Huaibo Huang, Ran He, Zhenan Sun, Tieniu Tan, et al. Introvae: Introspective variational autoencoders for photographic image synthesis. In *Advances in neural information processing systems*, pages 52–63, 2018.
- [22] Sergey Ioffe and Christian Szegedy. Batch normalization: Accelerating deep network training by reducing internal covariate shift. In *International conference on machine learning*, pages 448–456. PMLR, 2015.
- [23] Avinash C Kak, Malcolm Slaney, and Ge Wang. Principles of computerized tomographic imaging, 2002.

- [24] Tero Karras, Timo Aila, Samuli Laine, and Jaakko Lehtinen. Progressive growing of gans for improved quality, stability, and variation. *arXiv preprint arXiv:1710.10196*, 2017.
- [25] Diederik P Kingma and Jimmy Ba. Adam: A method for stochastic optimization. 3rd international conference on learning representations, iclr 2015. *arXiv preprint arXiv:1412.6980*, 9, 2015.
- [26] Diederik P Kingma, Tim Salimans, Rafal Jozefowicz, Xi Chen, Ilya Sutskever, and Max Welling. Improving variational inference with inverse autoregressive flow. *arXiv preprint arXiv:1606.04934*, 2016.
- [27] Diederik P. Kingma and Max Welling. Auto-encoding variational bayes. In Yoshua Bengio and Yann LeCun, editors, *2nd International Conference on Learning Representations, ICLR 2014, Banff, AB, Canada, April 14-16, 2014, Conference Track Proceedings*, 2014.
- [28] Diederik P. Kingma and Max Welling. An introduction to variational autoencoders. *Foundations and Trends® in Machine Learning*, 12(4):307–392, 2019.
- [29] Alexander Krull, Tim-Oliver Buchholz, and Florian Jug. Noise2void-learning denoising from single noisy images. In *Proceedings of the IEEE Conference on Computer Vision and Pattern Recognition*, pages 2129–2137, 2019.
- [30] Alexander Krull, Tomas Vicar, Mangal Prakash, Manan Lalit, and Florian Jug. Probabilistic Noise2Void: Unsupervised Content-Aware Denoising. *Front. Comput. Sci.*, 2:60, Feb. 2020.
- [31] Samuli Laine, Tero Karras, Jaakko Lehtinen, and Timo Aila. High-quality self-supervised deep image denoising. In *Advances in Neural Information Processing Systems*, pages 6968–6978, 2019.
- [32] Yann LeCun, Léon Bottou, Yoshua Bengio, and Patrick Haffner. Gradient-based learning applied to document recognition. *Proceedings of the IEEE*, 86(11):2278–2324, 1998.
- [33] Jaakko Lehtinen, Jacob Munkberg, Jon Hasselgren, Samuli Laine, Tero Karras, Miika Aittala, and Timo Aila. Noise2noise: Learning image restoration without clean data. *arXiv preprint arXiv:1803.04189*, 2018.
- [34] Valentin Liévin, Andrea Dittadi, Lars Maaløe, and Ole Winther. Towards hierarchical discrete variational autoencoders. 2019.
- [35] Lars Maaløe, Marco Fraccaro, Valentin Liévin, and Ole Winther. Biva: A very deep hierarchy of latent variables for generative modeling. *arXiv preprint arXiv:1902.02102*, 2019.
- [36] Ilja Manakov, Markus Rohm, Christoph Kern, Benedikt Schworm, Karsten Kortuem, and Volker Tresp. Noise as domain shift: Denoising medical images by unpaired image translation. In *Domain Adaptation and Representation Transfer and Medical Image Learning with Less Labels and Imperfect Data*, pages 3–10. Springer, 2019.
- [37] Peyman Milanfar. A tour of modern image filtering: New insights and methods, both practical and theoretical. *IEEE signal processing magazine*, 30(1):106–128, 2012.
- [38] Sreyas Mohan, Zahra Kadkhodaie, Eero P. Simoncelli, and Carlos Fernandez-Granda. Robust and interpretable blind image denoising via bias-free convolutional neural networks. In *International Conference on Learning Representations*, 2020.
- [39] Guy Ohayon, Theo Adrai, Gregory Vaksman, Michael Elad, and Peyman Milanfar. High perceptual quality image denoising with a posterior sampling cgan. *arXiv preprint arXiv:2103.04192*, 2021.
- [40] Mangal Prakash, Alexander Krull, and Florian Jug. Fully unsupervised diversity denoising with convolutional variational autoencoders. In *International Conference on Learning Representations*, 2021.
- [41] Mangal Prakash, Manan Lalit, Pavel Tomancak, Alexander Krull, and Florian Jug. Fully unsupervised probabilistic noise2void. *arXiv preprint arXiv:1911.12291*, 2019.
- [42] Yuhui Quan, Mingqin Chen, Tongyao Pang, and Hui Ji. Self2self with dropout: Learning self-supervised denoising from single image. In *Proceedings of the IEEE/CVF Conference on Computer Vision and Pattern Recognition*, pages 1890–1898, 2020.
- [43] GR Ramesh, N Srinivasa, and K Rajgopal. An algorithm for computing the discrete radon transform with some applications. In *Fourth IEEE Region 10 International Conference TENCON*, pages 78–81. IEEE, 1989.
- [44] Danilo Jimenez Rezende, Shakir Mohamed, and Daan Wierstra. Stochastic backpropagation and approximate inference in deep generative models. *arXiv preprint arXiv:1401.4082*, 2014.
- [45] Yaniv Romano, Michael Elad, and Peyman Milanfar. The little engine that could: Regularization by denoising (red). *SIAM Journal on Imaging Sciences*, 10(4):1804–1844, 2017.
- [46] Stefan Roth and Michael J Black. Fields of experts: A framework for learning image priors. In *2005 IEEE Computer Society Conference on Computer Vision and Pattern Recognition (CVPR'05)*, volume 2, pages 860–867. IEEE, 2005.
- [47] Leonid I Rudin, Stanley Osher, and Emad Fatemi. Nonlinear total variation based noise removal algorithms. *Physica D: nonlinear phenomena*, 60(1-4):259–268, 1992.
- [48] Casper Kaae Sønderby, Tapani Raiko, Lars Maaløe, Søren Kaae Sønderby, and Ole Winther. Ladder variational autoencoders. *arXiv preprint arXiv:1602.02282*, 2016.
- [49] Nitish Srivastava, Geoffrey Hinton, Alex Krizhevsky, Ilya Sutskever, and Ruslan Salakhutdinov. Dropout: a simple way to prevent neural networks from overfitting. *The journal of machine learning research*, 15(1):1929–1958, 2014.
- [50] Carlo Tomasi and Roberto Manduchi. Bilateral filtering for gray and color images. In *Sixth international conference on computer vision (IEEE Cat. No. 98CH36271)*, pages 839–846. IEEE, 1998.
- [51] Dmitry Ulyanov, Andrea Vedaldi, and Victor Lempitsky. Deep image prior. In *Proceedings of the IEEE Conference on Computer Vision and Pattern Recognition*, pages 9446–9454, 2018.
- [52] Arash Vahdat and Jan Kautz. Nvae: A deep hierarchical variational autoencoder. *arXiv preprint arXiv:2007.03898*, 2020.
- [53] Martin Weigert, Loïc Royer, Florian Jug, and Gene Myers. Isotropic reconstruction of 3D fluorescence microscopy images using convolutional neural networks. *arXiv*, Apr. 2017.

- [54] Martin Weigert, Uwe Schmidt, Tobias Boothe, Andreas Müller, Alexandr Dibrov, Akanksha Jain, Benjamin Wilhelm, Deborah Schmidt, Coleman Broaddus, Siân Culley, et al. Content-aware image restoration: pushing the limits of fluorescence microscopy. *Nature methods*, 15(12):1090–1097, 2018.
- [55] Yaochen Xie, Zhengyang Wang, and Shuiwang Ji. Noise2same: Optimizing a self-supervised bound for image denoising. *arXiv preprint arXiv:2010.11971*, 2020.
- [56] Kai Zhang, Wangmeng Zuo, Yunjin Chen, Deyu Meng, and Lei Zhang. Beyond a gaussian denoiser: Residual learning of deep cnn for image denoising. *IEEE Transactions on Image Processing*, 26(7):3142–3155, 2017.
- [57] Daniel Zoran and Yair Weiss. From learning models of natural image patches to whole image restoration. In *2011 International Conference on Computer Vision*, pages 479–486. IEEE, 2011.

A. Datasets and Training Details

A.1. Datasets Corrupted with Pixel-wise Noise

We consider two microscopy datasets namely, the (i) *FU-PN2V Convallaria* dataset from [30, 41] which shows 1024×1024 images of a intrinsically real-world noisy *Convallaria* sections, and the (ii) *DenoiSeg Flywing* dataset from [10], showing images of a developing Flywing. Following [40], we synthetically corrupted *DenoiSeg Flywing* images with zero mean Gaussian noise of standard deviation 70. The train and validation splits for these datasets are as described in the respective publication. For the *FU-PN2V Convallaria* dataset, the test set consists of 100 images of size 512×512 while the test set for *DenoiSeg Flywing* dataset consists of 42 images of size 512×512 .

From the domain of natural images, we consider two grayscale test datasets namely, (iii) the popular *BSD68* dataset from [46] containing 68 natural images of different sizes, and (iv) the *Set12* dataset from [56] containing 12 images of either size 512×512 or 256×256 . Both datasets have been synthetically corrupted with zero mean Gaussian noise of standard deviation 25. For training and validation, we use a set of 400 natural images of size 180×180 as released by [56] and has later also been used in [29].

Next, we chose to use (v) the popular *MNIST* dataset [32] showing 28×28 images of digits, and (vi) the *Kuzushiji-Kanji* dataset [14] showing 64×64 images of Kanji characters. Both datasets have been synthetically corrupted with zero mean Gaussian noise of standard deviation 140. For the Kanji dataset, we randomly select 119360 images for training and 14042 images for validation. The test set contains 100 randomly selected images not present in either training or validation sets. For the *MNIST* dataset, the publicly available data has two splits containing 60000 training images and 10000 test images. We further divide the training images into training and validation sets containing 54000 and 6000 images, respectively. We take a random subset of 100 images from the test data and use this as our test set to evaluate all methods. The noisy train, validation and test images for *Kanji* and *MNIST* data will be released publicly.

Finally, we selected two datasets of faces, namely, (vii) the *BioID Faces* dataset [1] showing 286×384 images of different persons under different lighting conditions, and (viii) the *CelebA HQ* dataset at 256×256 image resolution containing faces of celebrities from [24]¹. The *CelebA HQ* dataset has RGB images and we take only the red channel images for our experiments. Both facial datasets have been synthetically corrupted with zero mean Gaussian noise of standard deviation 15. For the *BioID Faces* dataset, we choose 340 images in the training set and 60 images in the validation set while the test set contains 100 additional images. For the *CelebA HQ* dataset, the train and validation sets contain 27000 and 1500 images, respectively, while the test set contains 100 additional images. We will release the noisy versions of these datasets publicly.

A.2. Datasets Corrupted with Structured Noises

We used the *BioID Faces* dataset for all our experiments with synthetic structured noises. In total, we generated four structured noises (sources of artefacts):

Chessboard patterns. We first corrupted the images with zero mean Gaussian noise with standard deviation 15. Following this, we went over each 8×8 pixel groups on each image and added a pixel-wise chessboard pattern on it uniform at random with probability ϵ . The added chessboard pattern is adding either -25 and $+25$ to the underlying image pixels.

Horizontal striping patterns. We first corrupted the images with zero mean Gaussian noise with standard deviation 7. Following this, we went over adjacent groups of 20×1 pixels and added a horizontal striping pattern with probability ϵ . The added horizontal pattern is obtained by convolving a 20×1 kernel (each element of the kernel having value $1/20$) with a noise vector of the same shape and the noise elements lying in the range $[0,60]$. Note, the added patterns are zero mean.

Moire patterns. We create an image of Moire patterns by the superposition of two sinusoidal waves with amplitudes 10. The first sinusoidal component has frequencies $45/\pi$ rad and $50/\pi$ rad in x and y directions, respectively. The second sinusoidal component has frequencies $-45/\pi$ rad and $50/\pi$ rad in x and y directions, respectively. Also, both components are phase shifted by π . We first corrupted our training images with zero mean Gaussian noise with standard deviation 15 and then added the Moire patterns uniform at random per-pixel with probability ϵ .

Computed Tomography (CT) artefacts. These artefacts are a consequence of how CT images are reconstructed from a given set of projections. We have used a CT simulator capable of projecting a given 2D image and then reconstructing a 2D image from these projections. Artefacts arise because a reconstruction based on too few projections suffers from missing data being observed. To create the data we used, we have cropped 283×283 tiles from each ground truth image in the respective training, validation and test sets. We used the CT simulator multiple times, each time specified a different number of projection angles, hence leading to artefacts of varying magnitude. More specifically, we choose 150, 180 and 200 projection angles for CT reconstruction.

¹The full dataset can be downloaded from the Google Drive link at <https://github.com/suvojit-0x55aa/celebA-HQ-dataset-download>

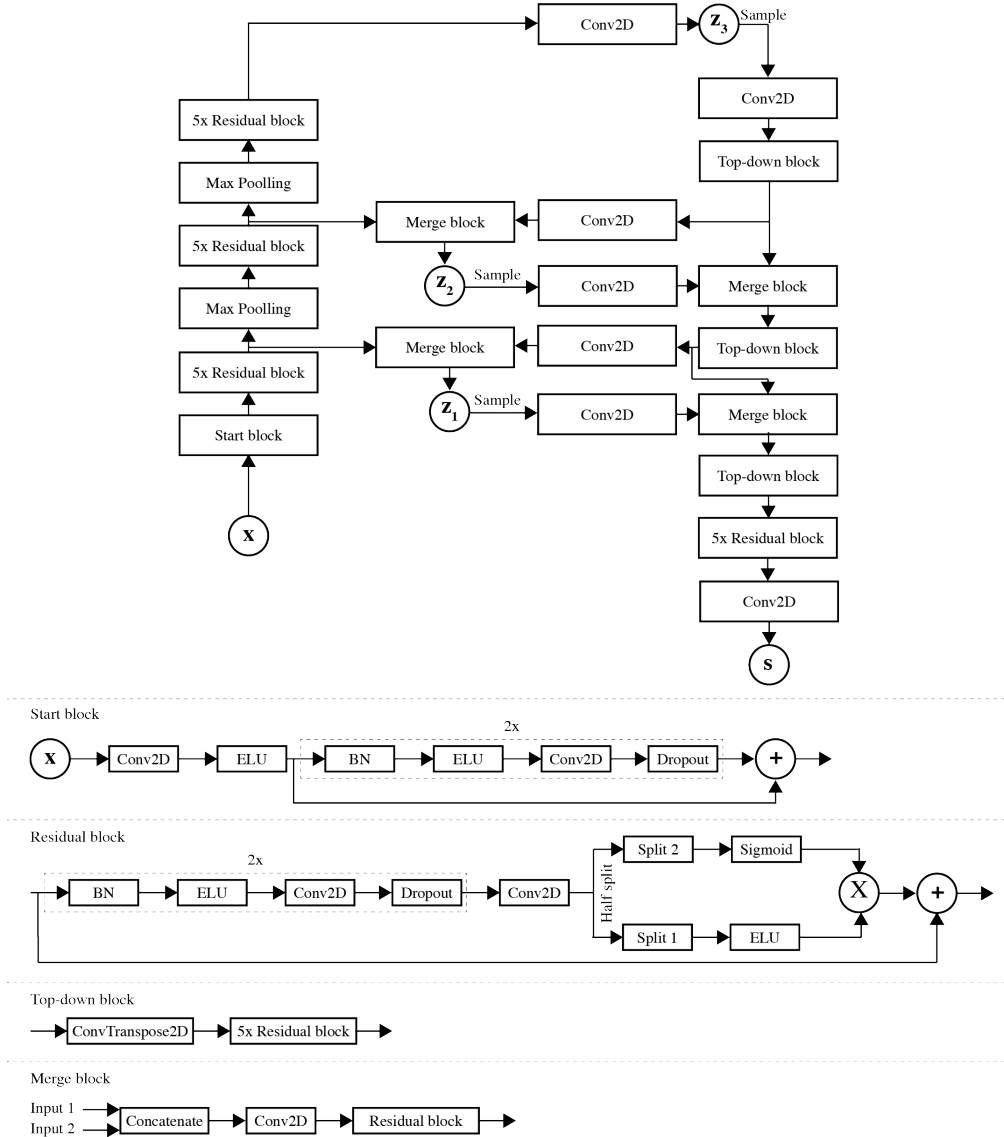


Figure A.1. **HIERARCHICAL DIVNOISING (HDN) network architecture.** The network architecture used for *MNIST* dataset is shown. For all other datasets, 6 stochastic latent groups are used instead of the 3 groups shown here.

A.3. Training details of Hierarchical DivNoising

Our HDN network is fully convolutional and consists of multiple hierarchical stochastic latent variables. For our experiments we use a network with 6 hierarchical latent variables, only for the *MNIST* dataset we have only used a hierarchy of height 3. Each latent group has $H_i \times W_i \times 32$ dimensions where H_i and W_i represent the dimensionality of the feature maps at layer i . The initial number of filters is set to 64 and we utilize batch-normalization [22] and dropout [49] with a probability of 0.2. Both *top-down* and *bottom-up* networks have 5 residual blocks between each latent group. A schematic of the residual blocks and the full network architecture is shown in Fig. A.1. A batch size of 16 was used for *BioID Faces* and *Natural* image datasets, while a batch size of 64 was used for *FU-PN2V Convallaria*, *DenoiSeg*

Flying, *Kanji* and *MNIST*. For the *CelebA HQ* dataset we used a batch size of 4. To prevent *KL vanishing* [3], we use the *free bits* approach as described in [26, 12]. For experiments on all datasets other than the *MNIST* dataset, we set the value of *free bits* to 1.0, while for the *MNIST* dataset a value of 0.5 was used.

A.4. Architecture of Hierarchical DivNoising

Figure A.1 shows our HIERARCHICAL DIVNOISING architecture with 3 stochastic latent variables, as used for experiments on the *MNIST* data. For all other experiments our architecture is the same, but has 6 latent variable groups instead of 3. Please note that we have used the exact same architecture for pixel-wise and structured noise removal experiments. Our networks with 6 latent groups need around 8 GB of GPU memory and were trained on a Titan Xp GPU. The training time until convergence varies from 1

day to 5 days depending on the task and dataset.

B. Median Estimate From HIERARCHICAL DIVNOISING Samples

Here, we compute the pixel-wise median estimate using 100 denoised samples from HIERARCHICAL DIVNOISING and compare it to the MMSE estimate as reported in Sec. 5. To compute the median estimate, we simply take the pixel-wise median of the 100 samples.

Dataset	HDN MMSE	HDN Median
Convallaria [41]	37.10	36.94
Flywing [10]	25.41	25.42
BSD68 [46]	28.70	28.43
Set12 [56]	29.80	29.72
BioID Faces [1]	34.61	34.57
CelebA HQ [24]	33.74	33.71
MNIST [32]	21.21	21.15
Kanji [14]	20.68	20.57

Table B.1. **Comparison of HDN MMSE estimate and HDN Median estimate.** We compare two point estimates namely MMSE and pixel-wise Median estimate obtained by using 100 HDN samples for all pixel-wise noise removal experiments. We observe that the MMSE estimate gives slightly better performance in terms of PSNR (in dB) compared to the Median estimate.

We observe in Table B.1 that the median estimate performs slightly worse than the MMSE estimate in terms of PSNR values. This is expected since MMSE estimate naturally minimizes the squared error and hence maximizes PSNR.

C. How Accurate is the HIERARCHICAL DIVNOISING posterior?

We qualitatively compare the learned posterior of HIERARCHICAL DIVNOISING with DIVNOISING. Since both methods are fully convolutional, we can generate images of arbitrary size. For the DIVNOISING setup, we sample from the unit normal Gaussian prior and for Hierarchical DIVNOISING, we sample from the learned priors as discussed in Sec. 4 and then generate results using the *top-down* network. Note that in either case, the images are generated by sampling the latent code from the prior without conditioning on an input image. Below, we show a random selection of generated images for *DenoiSeg Flywing*, *FU-PN2V Convallaria*, *Kanji*, *MNIST* and *natural images* datasets in Fig. C.2, Fig. C.3, Fig. C.4 and Fig. C.5, respectively.

When comparing generated images from both setups with real images from the respective datasets, it is rather evident that HIERARCHICAL DIVNOISING learns a much more accurate posterior of clean images than DIVNOISING. For the *MNIST*, *Kanji*, *FU-PN2V Convallaria* and *DenoiSeg Flywing* datasets, the images generated by HIERARCHICAL DIVNOISING have a very realistic appearance. For the *natural image* dataset the situation is rather different. Generated natural images do not have the same quality

as instances of the training dataset do, offering lots of room for future improvement. Hence, it appears that learning a suitable latent space encoding of clean natural images is much harder than for the other datasets.

D. Additional Qualitative Results for Structured Noise Removal

Here we show additional qualitative results obtained with DIVNOISING on images subjected to horizontal line artefacts or Moire patterns (see Fig. D.6). More specifically we show, as we did also in Section 6, how the abundance of structured noises, modulated by the ϵ fractions used during training, changes the restoration properties of trained networks. Like in the main text, used test images are either exposed to the highest level of structured noise ($\epsilon = 1$), or to inputs only being exposed to pixel-wise noise ($\epsilon = 0$). Additionally, we show very similar results in the context of computed tomography (CT), where reconstruction artefacts are removed by a vanilla VAE (see Fig. D.7). Note that CT artefacts are modulated by the number of projection angles used during CT reconstruction, thus, instead of ϵ , we study CT streaking artefact removal as a function of projection angles used during CT reconstruction.

E. Structured Noise Removal with GDD Methods vs. Supervised Baselines

We present a comparison of unsupervised GDD methods for structured noise/artefacts removal with the supervised methods NOISE2NOISE [33] and CARE [54] (see Table E.2). Due to having access to additional data, it is not surprising that both supervised methods outperform unsupervised GDD methods. However, depending on the structured noise, the NOISE2NOISE approach is not far ahead and has two decisive disadvantages. First, it requires more and specific paired training data, but maybe more importantly, it can and will only come up with one prediction while GDD approaches have the desired capability of sampling diverse data interpretations. The traditional supervised approach of CARE requires clean data during training, making a direct comparison even less fair. While, as we argue in the main text in great detail, GDD methods cannot apriori decide what spatial structures are signal and what others are artefacts, the paired training data for CARE makes this distinction very explicit.

Method	Chessboard	Horizontal	Moire
$DN_{\epsilon = 0.01}$	33.22	35.11	32.91
$DN_{\epsilon = 0.03}$	33.04	34.98	33.08
$DN_{\epsilon = 0.05}$	33.06	35.04	32.93
$DN_{\epsilon = 0.10}$	33.05	34.80	32.85
$DN_{\epsilon = 0.50}$	32.97	34.76	28.64
$DN_{\epsilon = 1.0}$	19.59	34.10	26.63
$N2N_{\epsilon = 0.01}$	34.80	35.35	32.15
$N2N_{\epsilon = 0.03}$	34.59	36.06	32.15
$N2N_{\epsilon = 0.05}$	33.84	35.95	32.82
$N2N_{\epsilon = 0.10}$	31.29	36.27	32.89
$N2N_{\epsilon = 0.50}$	24.92	36.97	30.63
$N2N_{\epsilon = 1.0}$	19.76	36.84	26.94
$CARE_{\epsilon = 0.01}$	33.69	35.94	32.22
$CARE_{\epsilon = 0.03}$	35.12	35.49	32.21
$CARE_{\epsilon = 0.05}$	35.09	35.97	31.63
$CARE_{\epsilon = 0.10}$	35.02	36.13	32.92
$CARE_{\epsilon = 0.50}$	34.94	34.78	34.89
$CARE_{\epsilon = 1.0}$	35.17	36.01	35.20
test input:	200 pas	180 pas	150 pas
VAE_{200}	41.21	40.65	38.79
VAE_{180}	41.32	40.59	38.60
VAE_{150}	41.44	40.48	38.16
$CARE_{200}$	44.32	42.55	38.40
$CARE_{180}$	45.69	44.75	40.52
$CARE_{150}$	45.27	44.73	43.12

Table E.2. **Structured noise removal with GDDs.** Top 6 rows show DIVNOISING (DN) results on the *BioID-Faces* dataset, subjected to 3 sources of structured noises (see Sec. 6 for details). Rows differ by the abundance (ϵ -fraction) of structured noise used during training. All results are evaluated on test-inputs generated at maximum artefact abundance ($\epsilon = 1$). The next two groups of 6 rows indicate the results of the supervised methods Noise2Noise [33] and CARE [54], respectively. The 6 bottom-most rows compare results of CARE, and vanilla VAEs trained on tomographic reconstructions from either 150, 180, or 200 projection angles (pas), also indicated as subscript in column 1. All numbers indicate PSNR values w.r.t. available ground truth images. As expected, supervised CARE method gives the best results in all categories.

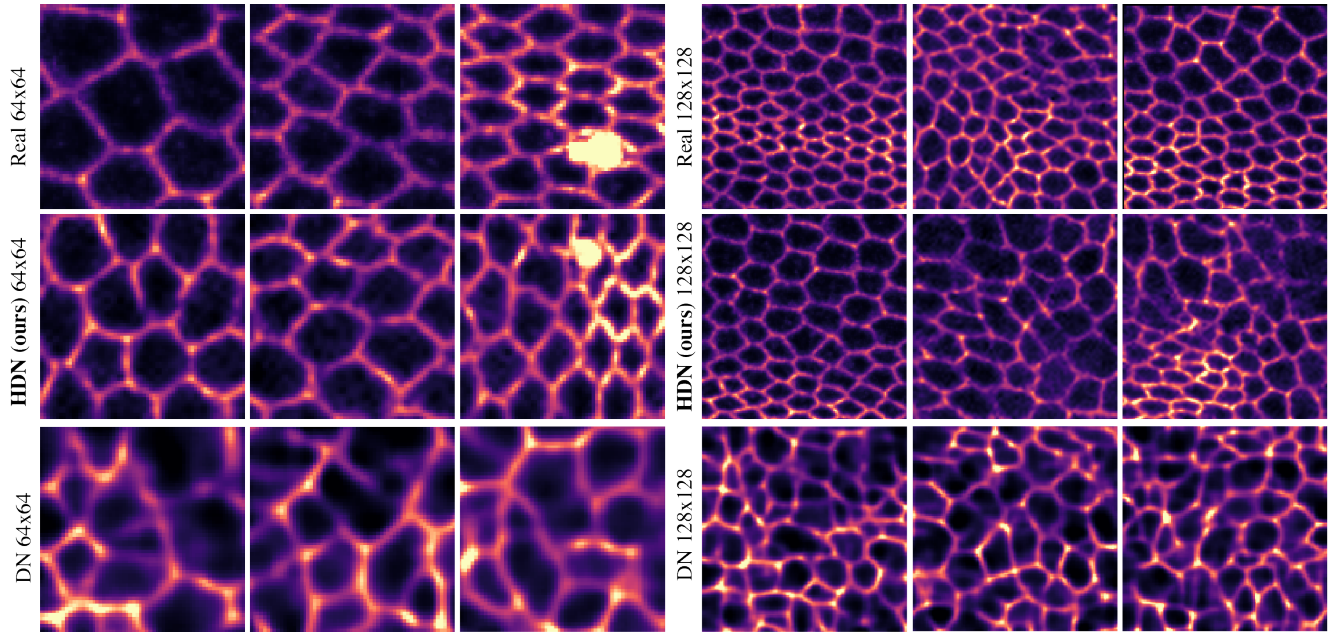


Figure C.2. **Accuracy of the learned posterior.** We show real images (*top row*), generated images from HIERARCHICAL DIVNOISING (*middle row*) and generated images from DIVNOISING (*bottom row*) at different resolutions for the *DenoiSeg Flywing* dataset. The images from our method look much more realistic compared to those generated by DIVNOISING, thereby validating the fact that our method learns a much better posterior distribution of clean images compared to DIVNOISING.

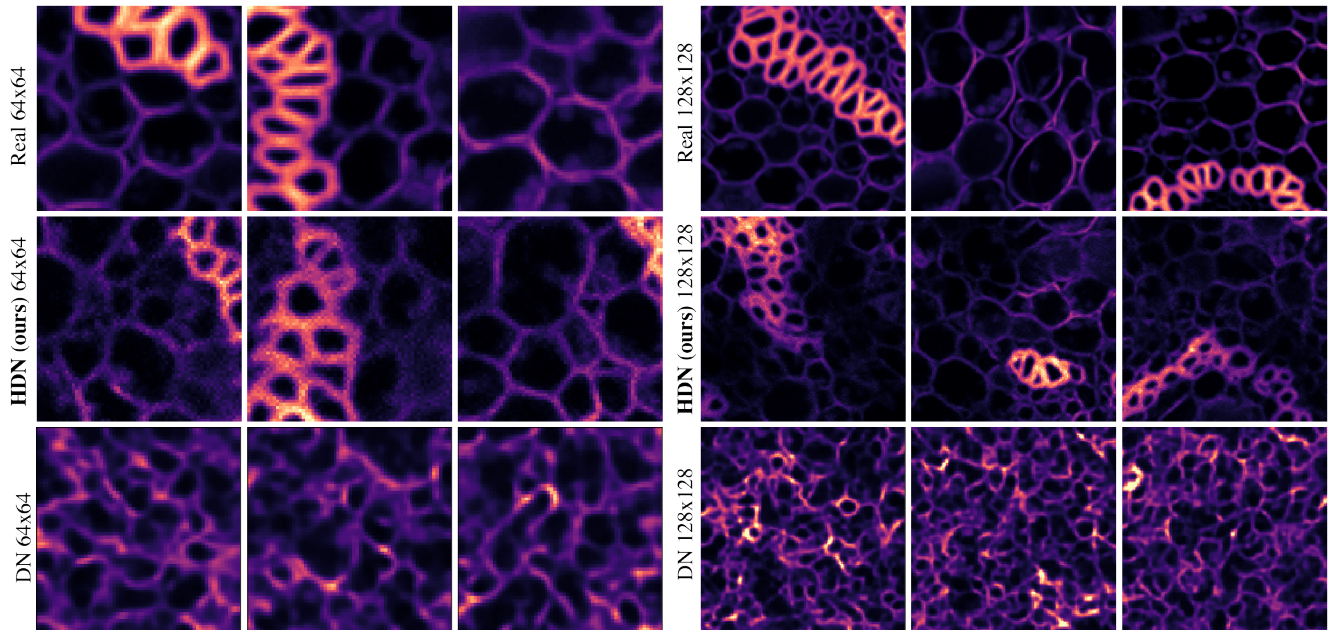


Figure C.3. **Accuracy of the learned posterior.** We show real images (*top row*), generated images from HIERARCHICAL DIVNOISING (*middle row*) and generated images from DIVNOISING (*bottom row*) at different resolutions for the *FU-PN2V Convallaria* dataset. The images from our method look much more realistic compared to those generated by DIVNOISING, thereby validating the fact that our method learns a much better posterior distribution of clean images compared to DIVNOISING.

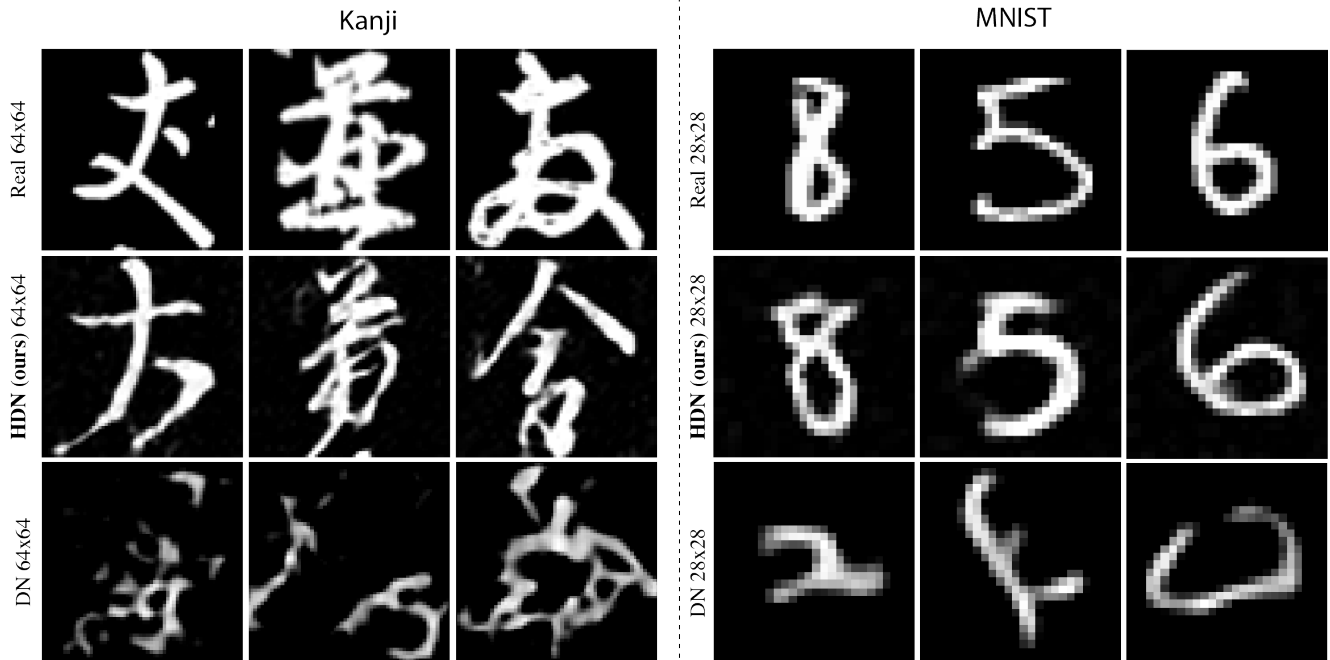


Figure C.4. **Accuracy of the learned posterior.** We show real images (*top row*), generated images from HIERARCHICAL DIVNOISING (*middle row*) and generated images from DIVNOISING (*bottom row*) for the *Kanji* dataset in first half and the *MNIST* dataset in second half. The images from our method look much more realistic compared to those generated by DIVNOISING, thereby validating the fact that our method learns a much better posterior distribution of clean images compared to DIVNOISING.

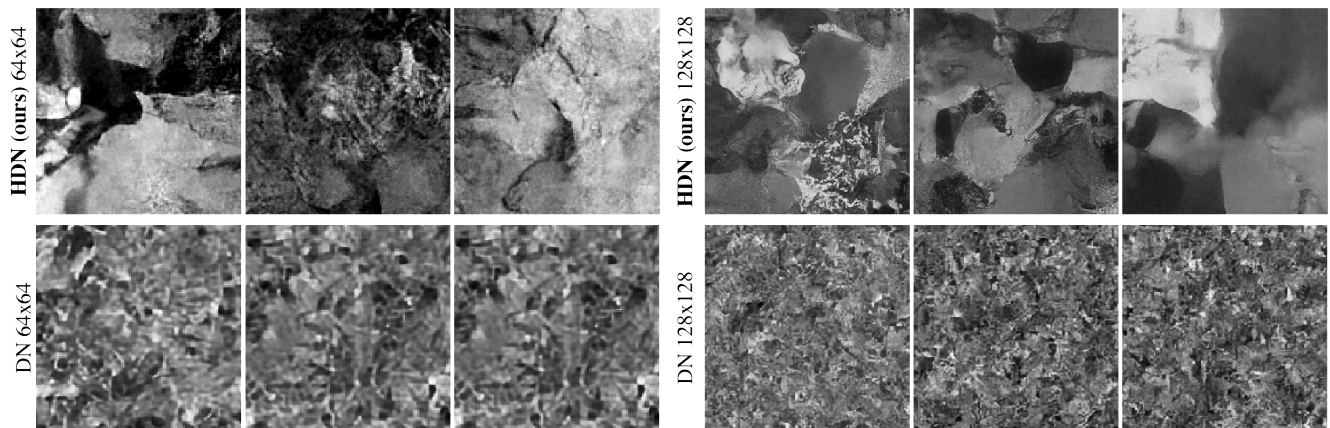


Figure C.5. **Accuracy of the learned posterior.** We show generated images from HIERARCHICAL DIVNOISING (*top row*) and generated images from DIVNOISING (*bottom row*) at different resolutions for *natural images*. The images from our method look much more realistic compared to those generated by DIVNOISING, although there seems to be plenty of room for improvement. The generated images by HDN vaguely resemble structures such as rock, clouds, etc. More meaningful structures like people, animals, etc. are not generated at all. This indicates that our method is not powerful enough to capture the tremendous diversity in natural image datasets but still gives SOTA denoising performance on natural image benchmarks (see Table 1 and Table I.4).

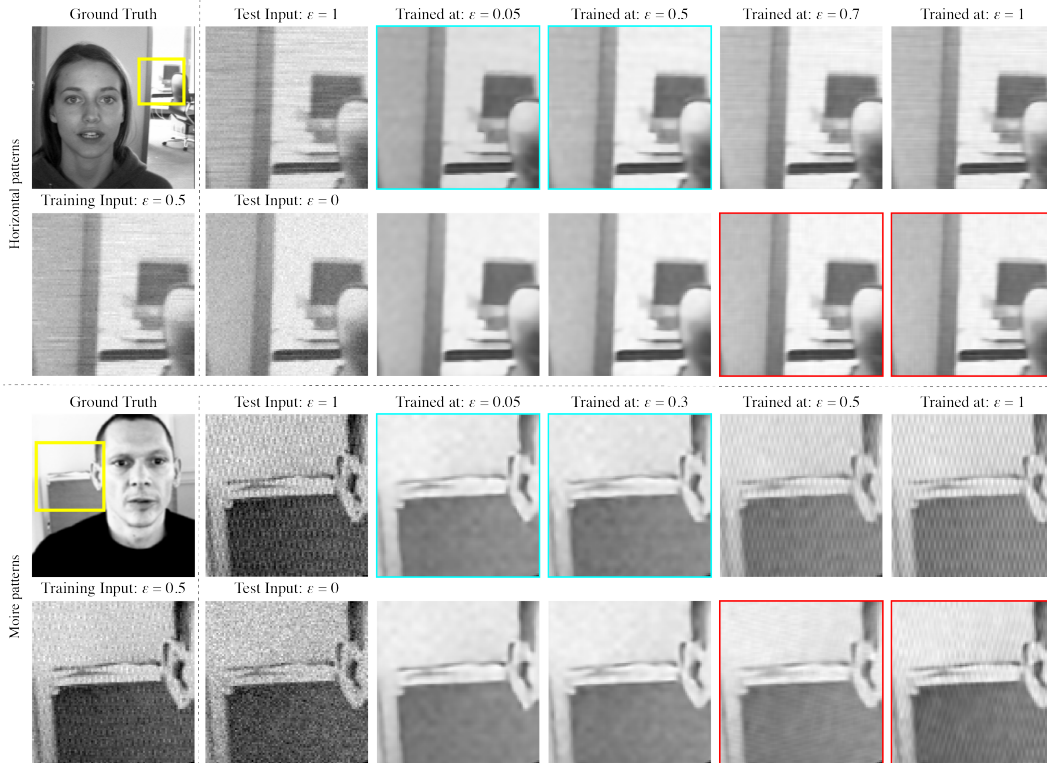


Figure D.6. **Testing structured noise removal with DIVNOISING at changing artefact abundance.** The top half shows results for horizontal pattern removal and the bottom half for the restoration of images corrupted with Moire patterns. The first column shows a ground truth image and below a crop of a training image subject to Gaussian and structured noise ($\epsilon = 0.5$). The second column shows two test inputs, top with highest abundance ($\epsilon = 1$), bottom without structured noise ($\epsilon = 0$). The remaining 4 columns show results obtained with DIVNOISING networks trained on input data exposed to various abundances ϵ . Cyan frames in the top row indicate cases where DIVNOISING successfully removes structured noise. Red frames, in the bottom row, indicate cases where restorations show structured noise patterns despite the input not containing them (hallucinated artefacts).

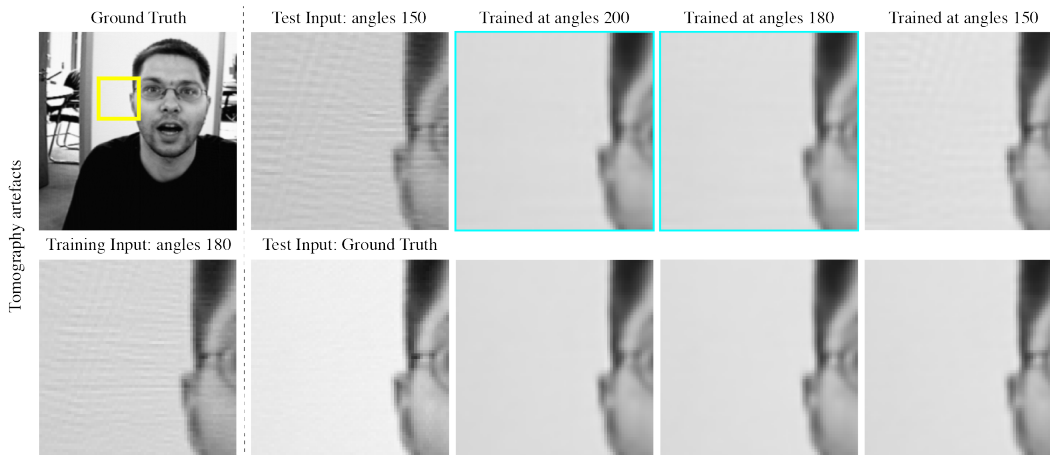


Figure D.7. **Testing tomography artefact removal with vanilla VAEs with varying abundance of artefacts.** The first column shows a ground truth image and below a crop of a training image subject to computational tomography (CT) artefacts simulated by using only 180 projection angles for reconstruction. The second column shows two test inputs, the top one with the artefacts simulated by using 150 projection angles, while the one below does not contain this structured noise at all (ground truth). The remaining 4 columns show results obtained with vanilla VAE networks trained on input data exposed to tomography artefacts due to reconstruction with different number of projection angles. Cyan frames in the top row indicate cases where the vanilla VAE successfully removes the artefacts. The bottom row indicates denoising results for the same networks when the corresponding input does not contain artefacts.

F. Visualizing Patterns Encoded by HDN Latent Layers and Targeted Deactivation

In this section we present a way to visualize what the individual levels of a HDN learned to represent. The idea for this way of inspecting a Ladder VAE is not new and can also be found in a GitHub repo² authored by a member of the team around [34].

More specifically, we want to visualize what our 6-layered HDN model has learned in Section 6 of the main text. We inspect layer i by performing the following steps:

- We draw a sample from all latent variables for layers $j > i$.
- We then draw 6 samples from layer i (conditioned on the samples we drew just before).
- For each of these 6 samples, we take the mean of the conditional distributions at layers $k < i$, *i.e.* we do not sample for these layers.
- We generate a total of 6 images given the latent variable samples and means from above.

The results of this procedure on the HDN network used in Section 6 can be seen in Fig. F.8.

Method	PSNR (dB)
HDN	29.78
HDN ₂₋₆	31.24
HDN ₃₋₆	31.36
HDN ₄₋₆	28.13

Table F.3. **Performance of HDN networks with “deactivated” latent layers.** We show results for HDN setups (in terms of PSNR) with different layers of the original HDN architecture “deactivated” (see Appendix F for how latent layers are deactivated). In line with our observations in Fig. F.8, the HDN₃₋₆ setup leads to the best performance on the data of [4], which we used here.

By visually inspecting Fig. F.8 one can observe that the bottom two layers (layers 1 and 2) learned fine details, including the line artefacts we would like to remove from input images. The other layers (layers 3 to 6), on the other hand, either learn smoother global structures or learn such abstracted concepts that the used visualization method is not very informative.

Still, the created visuals help us to understand why the full HDN leads to worse results for removing microscopy line artefacts than a DN setup did (see Table 2 in the main text). Owing to the high expressivity of the HDN model, the structured noise can actually be encoded in the hierarchical latent spaces and the artefacts will therefore be faithfully be represented in the otherwise denoised resulting image.

Motivated by these observations, we proposed a simple modification to HDN that has then led to SOTA results on the given benchmark dataset (see again Table 2 in the main text). We showed that by “deactivating” layers 1 and 2, *i.e.* the ones that show artefact-like patterns in Fig. F.8, the modified HDN model restored the data well and removed pixel noises as well as the undesired line artefacts (structured noise).

²<https://github.com/addtt/ladder-vae-pytorch>

Here, instead, we also computed results by “deactivating” only the bottom-most layer (HDN₂₋₆), the lowest two layers as described in the main text (HDN₃₋₆), and the bottom-most three layers (HDN₄₋₆). All results are shown in terms of peak signal-to-noise ratio (PSNR) in Table F.3. The best results are obtained with HDN₃₋₆ setup.

G. Early Stopping of HDN Training

As reported in Section 6 and Appendix F, we show that unaltered GDD networks, if expressive enough to encode given structured noises, might not remove them. However, we observed that early stopping can also help in these situations to remove structured noises since GDD models encode for the structures of interest (we wish to preserve) first before starting to encode for structured noise (we wish to remove). In Figure G.9 we show results obtained with a vanilla VAE, trained on computed tomography data, at various intermediate states of training.

Note that similar observation has been made in the Deep Image Prior (DIP) work [51].

H. Visualizing GDD Operations

Here we will first introduce a method to visualize what operation a trained GDD network carries out on a given input image. We will then use this method to get a deeper look “behind the scenes” of two DN networks. Both networks are trained on images that are subjected to synthetic Moire patterns, one below the *encoding threshold* for this dataset ($\varepsilon = 0.01$), the other above ($\varepsilon = 1$).

The visualization we propose to use is based on an idea we found in [38]. More specifically, we take a linear approximation of our non-linear denoising network f_ψ by computing its Jacobian (J) evaluated for input x . We then perform a Singular Value Decomposition (SVD) on the computed Jacobian. In Fig. H.10 we show examples of singular vectors of the Jacobians of the two trained networks.

When browsing through the singular vectors obtained with this method one notices that patterns that resemble the unwanted Moire patterns are either completely absent (for the network trained with $\varepsilon = 0.01$), or visible for all dominant (*i.e.* all of at least the first 1000) singular vectors (for the network trained with $\varepsilon = 1.0$). These observations suggest that there is indeed a sharp transition between latent encodings learned below or above the *encoding threshold*.

I. Pixel-wise Denoising in Terms of SSIM

While we have measured pixel-denoising performance in the main text in terms of PSNR, here we quantify all results also in terms of Structural Similarity (SSIM), see Table I.4.

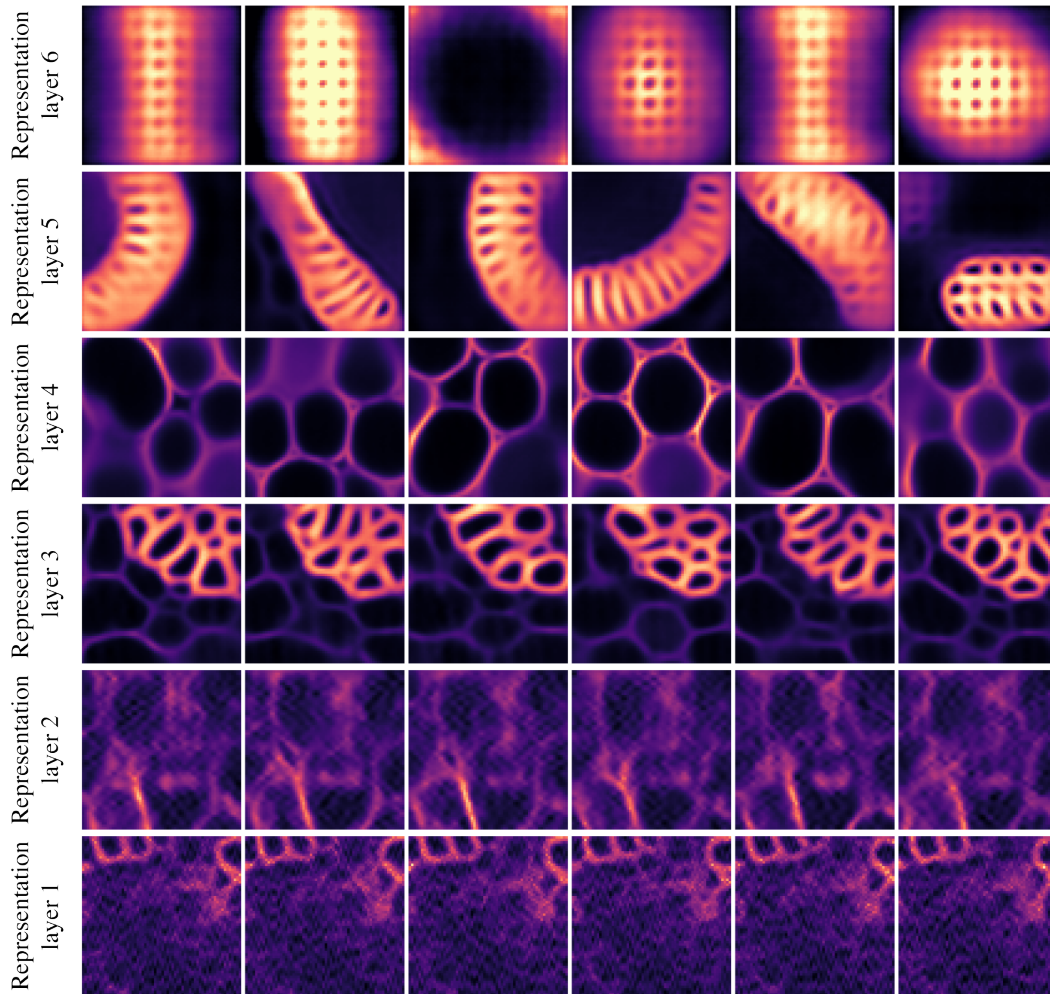


Figure F.8. **Visualizing what HIERARCHICAL DIVNOISING encodes at each latent layer.** Please see Appendix F for a detailed description of how the shown images have been created. The interesting observation is that structures that resemble the structured line artefacts are only visible in layers 1 and 2, which gave rise to the proposed HDN₃₋₆ network used in Tables 2 and F.3.

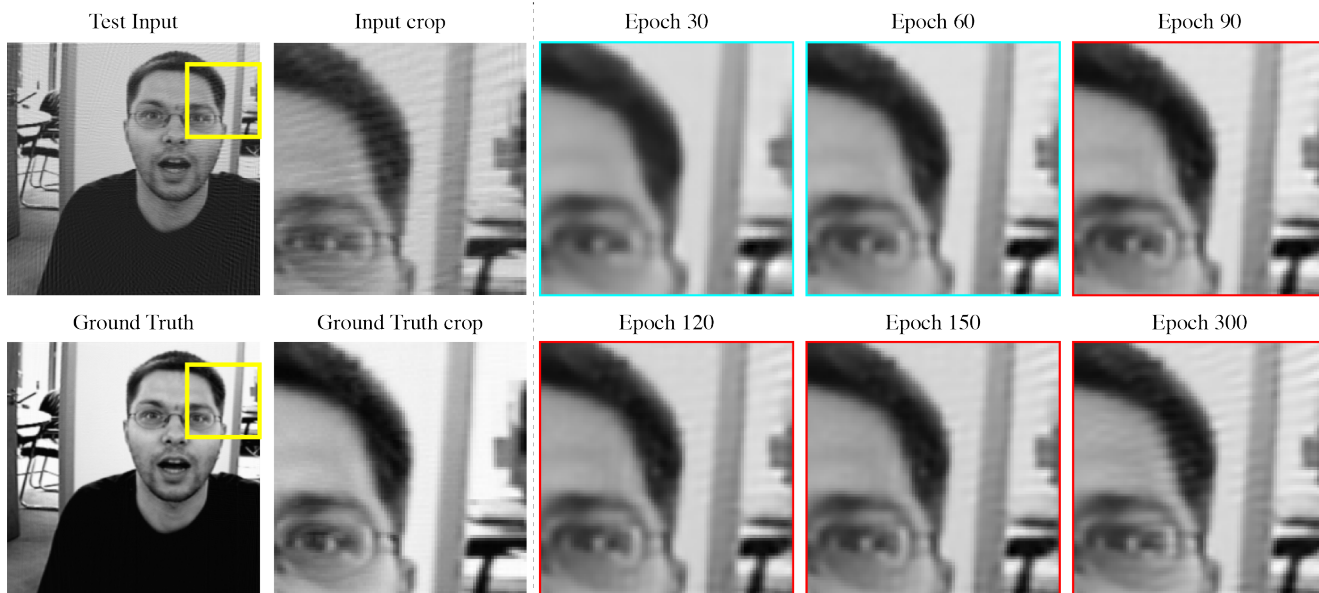


Figure G.9. **Inductive Bias of GDD Network.** We show that vanilla VAE has a strong inductive bias towards learning the structures of interest that we wish to retain compared to the structured noise/artefacts that we wish to discard. The first column shows a test image corrupted with computational tomography (CT) artefacts image and below the corresponding Ground Truth image. The second column shows a cropped region while the results of a VAE network at different time intervals during training with inputs containing CT artefacts is shown in the next 3 columns. Cyan frames indicate training intervals where vanilla VAE does not encode for CT artefacts. Red frames indicate training intervals when vanilla VAE starts encoding for artefacts. The artefacts are only encoded after encoding for the signals of interest.

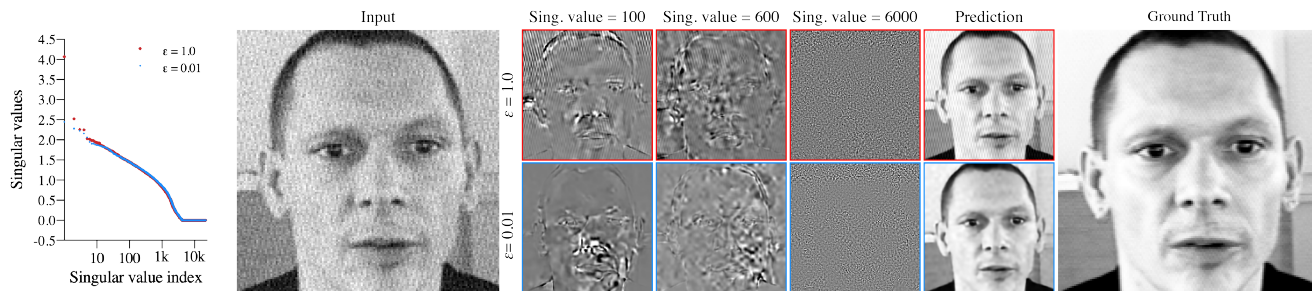


Figure H.10. **Visualizing the restoration behavior of GDD for structured noise removal.** We consider two DIVNOISING networks trained with inputs corrupted with Gaussian noise superimposed with Moire patterns at abundance fractions of $\epsilon = 0.01$ and $\epsilon = 1.0$. We look at the singular vectors of Jacobian matrices of both networks at the shown test image. Even the dominant singular vectors (corresponding to index 100 and 600 for network trained with $\epsilon = 1.0$ setup encode for Moire patterns while this is not the case for network trained with $\epsilon = 0.01$ setup. The weaker singular vectors for both setups encode for pixel-wise noise.

SSIM										
Dataset	Non DL	Single Image DL		Multi Image DL (non-GDD)			GDD Methods		Supervised	
	BM3D	DIP	S2S	N2V	Noise2Same	PN2V	DN	HDN (Ours)	N2N	CARE
Convallaria [41]	0.939	-	-	0.954	0.963	0.959	0.966	0.966	0.963	0.962
Flying [10]	0.721	-	-	0.843	0.482	0.821	0.842	0.852	0.865	<u>0.866</u>
BSD68 [46]	0.801	0.774	0.803	0.778	0.776	0.801	0.754	0.812	0.812	<u>0.827</u>
Set12 [56]	0.850	0.772	0.832	0.828	0.818	0.831	0.787	0.837	0.844	<u>0.860</u>
BioID Faces [1]	0.909	-	-	0.865	0.907	0.891	0.886	0.920	<u>0.920</u>	0.919
CelebA HQ [24]	0.904	-	-	0.851	0.884	0.895	0.874	0.918	0.912	0.914
MNIST [32]	0.521	-	-	0.707	0.475	0.455	0.759	0.874	0.869	0.866
Kanji [14]	0.504	-	-	0.678	0.431	0.576	0.664	0.844	<u>0.891</u>	0.888
PSNR (in dB)										
Convallaria [41]	35.45	-	-	35.73	36.46	36.47	36.90	37.10	36.85	36.71
Flying [10]	23.45	24.67	-	24.79	22.81	24.85	25.02	25.41	25.67	<u>25.79</u>
BSD68 [46]	28.56	27.96	28.61	27.70	27.95	28.46	27.42	28.70	28.86	<u>29.07</u>
Set12 [56]	29.94	28.60	29.51	28.92	29.35	29.61	28.24	29.80	30.04	<u>30.36</u>
BioID Faces [1]	33.91	-	-	32.34	34.05	33.76	33.12	34.61	35.04	<u>35.06</u>
CelebA HQ [24]	33.28	-	-	30.80	31.82	33.01	31.41	33.74	33.39	33.57
MNIST [32]	15.82	-	-	19.04	18.79	13.87	19.06	21.21	20.29	20.43
Kanji [14]	20.45	-	-	19.95	20.28	19.40	19.47	20.68	20.56	20.64

Table I.4. **Quantitative pixel-noise removal with HDN.** For all conducted experiments, we compare results in terms of Structural Similarity (SSIM) and PSNR. The best performing method is indicated by being underlined, best performing unsupervised method is shown in bold. For all but one dataset, our HIERARCHICAL DIVNOISING is the new unsupervised SOTA method, even superseding the competing supervised baselines on 4 of the 8 used datasets.